Investigations on bubbly two-phase flow in a constricted vertical pipe

Neumann-Kipping, M.; Bieberle, A.; Hampel, U.;

Originally published:

May 2020

International Journal of Multiphase Flow 130(2020), 103340

DOI: https://doi.org/10.1016/j.ijmultiphaseflow.2020.103340

Investigations on bubbly two-phase flow in a constricted vertical pipe

Martin Neumann-Kipping[1], André Bieberle[2], Uwe Hampel[1,2]

[1] Chair of Imaging Techniques in Energy and Process Engineering, Technische Universität Dresden, 01062 Dresden, Germany

[2] Institute of Fluid Dynamics, Helmholtz-Zentrum Dresden - Rossendorf, Bautzner Landstraße. 400, 01328 Dresden, Germany

Abstract

We report on an experimental investigation of adiabatic bubbly two-phase flow development in a DN50 pipe with a ring-shaped and a baffle-shaped constriction at different superficial velocities of gas (up to j_g = 0.1400 m·s^{-1}) and liquid (up to j_l = 1.6110 m·s^{-1}) using ultrafast electron beam X-ray computed tomography (UFXCT). From UFXCT images, cross-sectional gas holdup distributions were obtained with a temporal resolution of up to 2,500 frames per second in 18 scanning planes along the pipe. A sophisticated data processing approach was applied to extract gas holdup data immediately from the two-phase flow image stack. Based on that, time-averaged gas holdup of the cross-section and the axial center of the pipe were calculated. In addition, bubble sizes and velocities were determined.

Key words: gas-liquid two-phase flow, bubbly flow, flow constriction, three-dimensional flow, computed tomography, experimental benchmark data

1 Introduction

Two-phase flows can be found in many industrial applications. Examples are multiphase chemical reactors, power plant circuits, heat exchangers or oil and gas production. Hence, there is a continuing interest in modelling and simulation. Computational fluid dynamics is the method of choice to simulate such flows at a high level of detail. However, for two-phase flow such simulation codes are yet not fully mature due to the inherent physical complexity of flows with phase boundaries. This holds especially for gas-liquid two-phase flow due to the deformability of gas-liquid interfaces. [1–3]. Thus, experimental validation is still inevitable. The particular challenge there, however, is the need to produce data with highest resolution in space and time, e.g. for transient flow phenomena.

Two phase flow in straight pipes of any inclination has been seen as a benchmark case for multiphase CFD for some years now. Hence, numerous experimental test cases are known from literature, e.g. for vertical upward flow [4–6], downward flow [7–9] or both flow directions [10–12], as well as horizontal flow [13–15]. A logical next step are benchmark cases for slightly more complex flow scenarios, such as constrictions, bends or junctions, with significant three-dimensional flow effects, such as flow separation at sharp edges, recirculation areas or curved streamlines. For the latter, however, only very few CFD-grade experimental data are available. One example is Prasser et al. [16] and Frank et al. [17], who investigated the flow around an axially moveable semicircular obstacle for a vertical pipe with an inner diameter of 195.3 mm using the wire-mesh sensor technique [18,19]. In these studies, the authors measured phase distributions and bubble sizes with a temporal resolution of 2,500 images per second for air-water and steam-water flow. From this, axial and lateral gas bubble velocities as well as time-averaged liquid velocities were estimated. The data was used for assessment and validation of CFD simulations with ANSYS CFX employing a multiple size group modelling approach for the gas phase [20]. The slight intrusiveness of the wire-mesh sensor and the driving mechanism of the obstacle as well as the 3 mm spatial resolution brought about increasing uncertainties for smaller bubbles and lower liquid velocities [21,22]. The present study aimed at the extension of the available experimental database for bubbly gas-liquid two-phase flow with a pronounced three-dimensional flow field. Experiments have been performed in a vertical pipe with an inner diameter of 53 mm. The impact of two different flow constrictions on the flow field were studied: a baffle-shaped and a ring-shaped type, respectively. The choice was made, because the baffle-shaped constriction creates an asymmetric flow field while the ring-shaped one creates an axially symmetric flow fields. This is useful to study different aspects of the flow, such as in-plane flow components. Hence, some comparability to already existing experimental data [16] is given for the baffle-shaped flow constriction. In addition, the ring-shaped flow constriction provides a true extension of the available database.

Experiments were performed using ultrafast X-ray computed tomography (UFXCT) [23,24]. It is a fast and non-invasive imaging technique for the investigation of highly transient processes, especially for bubbly two-phase flows [11,25–29]. With the applied temporal resolution of up to 2,500 images per second, the fluid dynamics could be studied without influencing the flow field. With this imaging technique we obtained quantitative parameters, such as total phase holdups, cross-sectional phase distributions, gas bubble sizes as well as their distributions and velocities. In the following we discuss only selected results. For access to the full data set the reader is referred to the RODARE Open Data Link given in [30,31].

2 Experimental setup

2.1 Vertical test section

Experiments are conducted in a vertical test section at the thermal-hydraulic test facility TOPFLOW (see Figure 1 a)) [30], [31]. Here, flow investigations have been performed under adiabatic conditions in an acrylic pipe with an inner diameter of

D = 53 mm and a total length of L = 4950 mm. Deionized water and compressed air were used as liquid and gas phase in co-current upward flow. Inlet flow rates are controlled by a volute pump (HPH 100-250, KSB, Germany) and a mass flow controller (F-202AC, Bronkhorst, Netherlands) for liquid and gas phase respectively. With this equipment we maintain a constant liquid temperature of 30°C and pressure of 4 bar at the gas injection at the bottom of the test section.

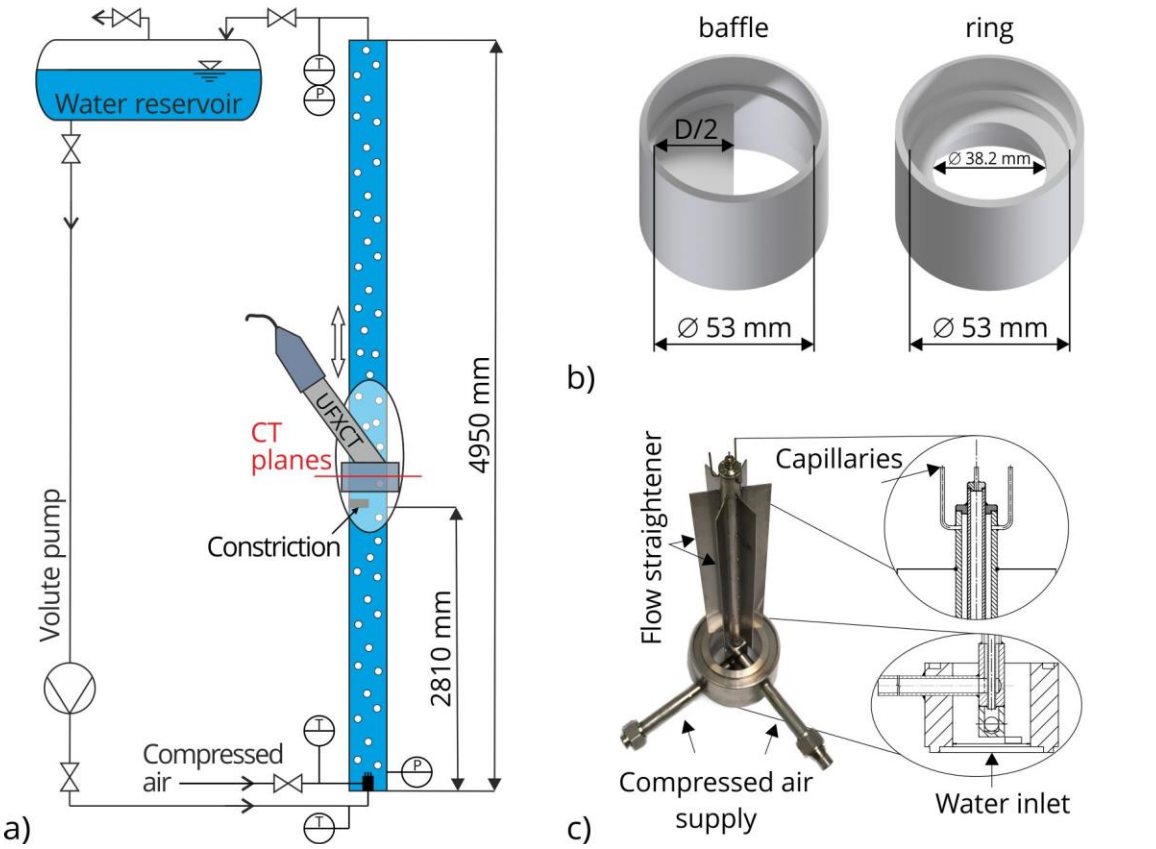

Figure 1: Schematic representations of the vertical obstructed test section showing a) the entire test section pipe connected to the (simplified and reduced depicted) TOPFLOW facility, b) the applied flow constrictions for generation of three-dimensional flow fields and c) the gas injection module.

Figure 1 b) shows both flow constrictions, the baffle-shaped and ring-shaped one. Both block exactly half of the inner pipe cross-section. Each obstacle is 5 mm thick and its bottom edge is at a distance of l = 2810 mm above the gas injector. That is, we have a length-to-diameter ratio of l/D = 52, for which we consider the two-phase flow as fully developed.

Figure 1 c) shows the gas injection module that was already used in previous studies, e.g. Banowski et al. for comparability study of UFXCT and wire-mesh sensor technique [22]. It mainly comprises four capillaries with an inner diameter of 0.8 mm and six equidistantly arranged metal sheets for straightening and homogenizing the liquid flow.

2.2 Ultrafast X-ray computed tomography

Ultrafast electron beam X-ray computed tomography (UFXCT) uses a deflected electron beam to produce a rapidly rotating X-ray spot. Along with a stationary multi-pixel dual-plane X-ray detector this configuration is used to scan tomographic projections of the flow. From these, cross-sectional images are reconstructed. Each image has a size of 180×180 pixels with a corresponding pixel size of 0.5 mm. The in-plane spatial resolution of the UFXCT scanner is nominally 1 mm. However, since gas-liquid flow has a specific contrast, we found in earlier studies that detection of single gas bubbles is secure only for bubbles with a dimeter of $d_B \geq 2$ mm. The two imaging planes of the UFXCT scanner offer a geometric distance of about 10 mm. The imaging speed in this study was up to 2,500 frames per second and per plane, depending on the expected flow velocity. For more details on general principles of computed tomography, the reader is referred to [34–36] and for more details on ultrafast X-ray computed tomography to [24,37,38].

The UFXCT scanner can be freely moved along the pipe with the help of an elevator mechanism. Hence it is possible to study the gas-liquid flow in any position up- and downstream of the flow constriction. The scanning planes used in this study are compiled in Table 1 as distances z of the upper and lower imaging plane with respect to the center of the flow constriction.

Table 1: Image plane identifiers along the vertical test section pipe and according distances z of the upper and lower UFXCT imaging plane to the center of the respective flow constriction. Additionally dimensionless distance-to-diameter ratios z/D are given.

Identifier	A	B	C	D	E	F	G	H	I
z [mm]	-200	-60	0	5	20	50	100	200	400
	-210	-70	-10	-5	10	40	90	190	390
z/D	-4	-1	0	0.1	0.5	1	2	4	8

2.3 Gas holdup

The raw tomographic data is a set of gray value images encoding the X-ray attenuation coefficient $\mu_{i,j,k}$ of a pixel with indices (i,j) and temporal index k. The conventional procedure to calculate gas holdup from UFXCT images is as follows: scans of the two-phase flow $\mu_{i,j,k}^{(\mathrm{tp})}$ and two k-averaged reference states, i.e. empty cross section $\bar{\mu}_{i,j}^{(\mathrm{gas})}$ and liquid filled cross section $\bar{\mu}_{i,j}^{(\mathrm{liq})}$, are used to calculate the gas holdup $\varepsilon_{i,j,k}$ according to

$$\varepsilon_{i,j,k} = \frac{\bar{\mu}_{i,j}^{(\mathrm{liq})} - \mu_{i,j,k}^{(\mathrm{tp})}}{\bar{\mu}_{i,j}^{(\mathrm{liq})} - \bar{\mu}_{i,j}^{(\mathrm{gas})}}. \tag{1}$$

This method has already been introduced by Zalucky et al. [39]. However, it was found that this method is sensitive to image artifacts from e.g. beam hardening, radiation scattering and geometrical dispositions of the deflected X-ray source and/or the object of investigation [40].

Therefore, an improved data processing procedure was developed. Here, the liquid reference data set $\bar{\mu}_{i,j}^{(\mathrm{liq})}$ and an estimation of the attenuation difference

$\bar{\mu}_{i,j}^{(\text{liq})}$ - $\bar{\mu}_{i,j}^{(\text{gas})}$ are directly extracted from the two-phase flow data $\mu_{i,j,k}^{(\text{tp})}$. The calculation comprises two main processing steps: a) a histogram calibration step from which the liquid reference data set $\bar{\mu}_{i,j}^{(\text{liq})}$ is obtained and b) an optimization step from which the attenuation difference $\bar{\mu}_{i,j}^{(\text{liq})}$ - $\bar{\mu}_{i,j}^{(\text{gas})}$ is estimated. This approach effectively suppresses adverse effects of image artifacts and non-linearities.

Figure 2 illustrates the first data processing step. Here, a histogram of all k reconstructed attenuation values $\mu_{i,j,k}^{(\text{tp})}$ is compiled for each image pixel (i, j). If the average gas holdup of the corresponding pixel (i, j) is around 50%, then its attenuation value distribution is typically bimodal (see Figure 2, bottom center). Though the gas and liquid phase in a two-phase flow have well-defined attenuation coefficients, the reconstructed values are corrupted by noise, artifacts and non-linearities. As the Poisson noise of the X-ray source and the Gaussian noise of the detectors are dominating we can assume a Gaussian distribution for both values. Hence, we extract average liquid $\mu_{\mu}^{(\text{liq})}$ and gas $\mu_{\mu}^{(\text{gas})}$ values from $\mu_{i,j,k}^{(\text{tp})}$ by fitting two Gaussian curves into the histogram. This is done for all image pixels.

As the liquid phase is dominant in our case of bubbly two-phase flow, $\mu_{\mu}^{(\text{liq})}$ can be determined with good accuracy. For $\mu_{\mu}^{(\text{gas})}$ it is more difficult, as its peak in the histogram is typically weak or even missing. Note, if gas phase would be dominate, e.g. for droplet flow, the situation would be vice versa.

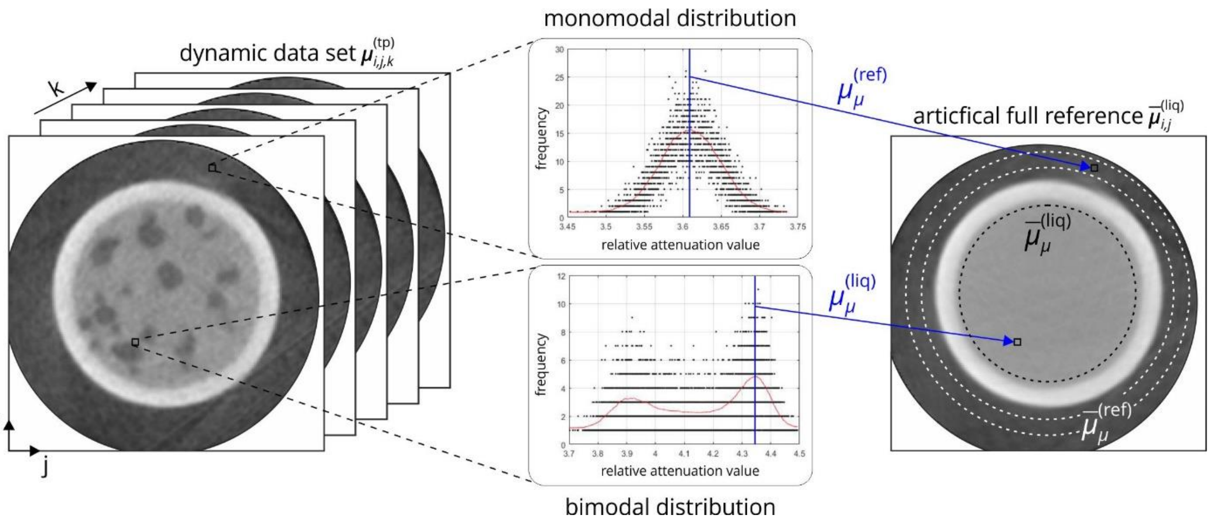

Figure 2: Schematic illustration to extract a full reference data set $\bar{\mu}^{(\mathrm{liq})}_{i,j}$ from the dynamic two-phase flow data set $\mu^{(\mathrm{tp})}_{i,j,k}$ based on a frequency distribution analysis of attenuation values at each image pixel (i, j).

Thus, the attenuation difference $\bar{\mu}^{(\mathrm{liq})}_{i,j}$ - $\bar{\mu}^{(\mathrm{gas})}_{i,j}$ is determined in a second data processing step. As illustrated in Figure 2 we may obtain $\bar{\mu}^{(\mathrm{gas})}_{i,j}$ from reference pixels with average value $\bar{\mu}^{(\mathrm{ref})}_{\mu}$ outside the column. However, as it can also be seen in Figure 2, the gas values in the bubble are on average slightly brighter which is caused by partial volume effects as well as beam scattering and beam hardening artifacts. Therefore, the sought value $\bar{\mu}^{(\mathrm{gas})}_{i,j}$ is obtained in the following way.

We set $\bar{\mu}^{(\mathrm{gas})}_{i,j} = \bar{\mu}^{(\mathrm{ref})}_{\mu}$, calculate the gas holdup according to Eq. (1) and compile the histogram (left side of Figure 3). As can be seen, the gas holdup maximum is $\varepsilon < 1$ while we would expect it to be $\varepsilon = 1$. Now, we fit a Gaussian distribution function to the right slope of the histogram and determine its mean value ε_m. Now the task is to find an appropriate average attenuation value for gas, which is larger than the reference value by an offset a, that is

$$\bar{\mu}^{(\mathrm{gas})}_{i,j} = \bar{\mu}^{(\mathrm{ref})}_{\mu} + a\,. \tag{2}$$

If this reference value shifts ε_m to 1, as we would expect, then Eq. (1) can be written as

$$\frac{\varepsilon_{i,j,k}}{\varepsilon_m} = \frac{1}{\varepsilon_m} \frac{\bar{\mu}_{i,j}^{(\text{liq})} - \mu_{i,j,k}^{(\text{tp})}}{\bar{\mu}_{i,j}^{(\text{liq})} - \bar{\mu}_{\mu}^{(\text{ref})}} = \frac{\bar{\mu}_{i,j}^{(\text{liq})} - \mu_{i,j,k}^{(\text{tp})}}{\bar{\mu}_{i,j}^{(\text{liq})} - \left(\bar{\mu}_{\mu}^{(\text{ref})} + a\right)}. \tag{3}$$

Setting $\Delta = \bar{\mu}_{i,j}^{(\text{liq})} - \bar{\mu}_{\mu}^{(\text{ref})}$ and solving for a yields

$$a = \Delta(1 - \varepsilon_m) \tag{4}$$

or by using Eq. (2)

$$\bar{\mu}_{i,j}^{(\text{gas})} = (1 - \varepsilon_m)\bar{\mu}_{i,j}^{(\text{liq})} + \varepsilon_m \, \bar{\mu}_{\mu}^{(\text{ref})}. \tag{5}$$

With this value for $\bar{\mu}_{i,j}^{(\text{gas})}$ we obtain the scaled histogram shown on the right side of Figure 3.

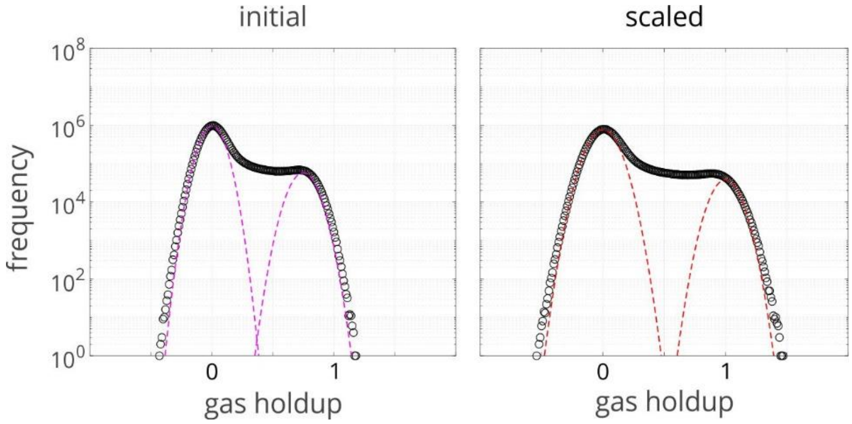

Figure 3: Gas holdup histogram calculated according to Eq. (1) using $\bar{\mu}_{\mu}^{(\text{ref})}$ (left) and $(1 - \varepsilon_m)\bar{\mu}_{i,j}^{(\text{liq})} + \varepsilon_m \, \bar{\mu}_{\mu}^{(\text{ref})}$ (right) as empty reference $\bar{\mu}_{i,j}^{(\text{gas})}$.

2.4 Gas phase parameters and bubble properties

From the $\varepsilon_{i,j,k}$ we can calculate the time-averaged cross-sectional gas phase distribution:

$$\bar{\varepsilon}_{i,j} = \frac{1}{N_k} \sum_{k=1}^{N_k} \varepsilon_{i,j,k} \tag{6}$$

as well as time- and space-averaged total gas holdup

$$\bar{\varepsilon} = \sum_{i=1}^{N_i} \sum_{j=1}^{N_j} w_{i,j} \cdot \bar{\varepsilon}_{i,j}. \tag{7}$$

Here $w_{i,j}$ are weights encoding the fraction of pixel area inside the pipe cross section. In a next step, we binarize $\varepsilon_{i,j,k}$ in order to discriminate gas from liquid. Thus, an iterative algorithm is applied which is based on a concept proposed by Banowski et al. [41]. Here, pixel clusters are identified as connected objects based on seed points of maximum gas holdup. This algorithm finally yields two data sets: a) a binarized data set $\varepsilon_{i,j,k}^{(\mathrm{bin})}$ containing values "1" and "0" for gas and liquid phase only and b) a corresponding identifier data set $\varepsilon_{i,j,k}^{(\mathrm{id})}$, containing individual bubble numbers. Furthermore, the bubble property analysis module of the wire-mesh sensor data processing software is used to extract bubble properties, e.g. bubble size and its position [42].

In the image stack, the axial dimension is time k. Hence, the identified bubble volume is given in mm²·ms. It is required to convert time into length measures, hence bubble volume needs to be multiplied by the axial gas phase velocity. To determine this velocity a cross-correlation function

$$F_{i,j,\Delta k} = \frac{\sum_{k=1}^{N_k} \varepsilon_{i,j,k}^{(\mathrm{low})} \cdot \varepsilon_{i,j,k}^{(\mathrm{up})}}{\sqrt{\sum_{k=1}^{N_k} \left(\varepsilon_{i,j,k}^{(\mathrm{low})}\right)^2 \cdot \sum_{k=1}^{N_k} \left(\varepsilon_{i,j,k}^{(\mathrm{up})}\right)^2}} \tag{8}$$

of the gas holdup is calculated for each pixel pair (i,j) of upper scanning plane $\varepsilon_{i,j,k}^{(\mathrm{up})}$ and lower scanning plane $\varepsilon_{i,j,k}^{(\mathrm{low})}$ separately. The index Δk corresponds to the time-shift $\Delta t = \Delta k / f$ with f being the image frequency per scanning plane. Then, the axial gas phase velocity map $\bar{u}_{i,j}^{(\mathrm{ax})}$ is calculated using the maximum of the cross-correlation function according to

$$\bar{u}_{i,j}^{(\mathrm{ax})} = \frac{\Delta m_{i,j}}{\Delta k_{i,j}^{(\mathrm{max})}} \cdot f \qquad \text{where} \qquad \Delta k_{i,j}^{(\mathrm{max})} = \arg\max_{k}\left(F_{i,j,\Delta k}\right). \tag{9}$$

Here, the unequal distribution of the effective imaging plane distance of the UFXCT scanner is taken into account by the distance map $\Delta m_{i,j}$ as introduced by Neumann et al. [43]. This allows for a position-dependent calculation of bubble sizes. This approach is typically valid only for unidirectional flow, which is, however, not the case in areas around the flow constrictions and in recirculation zones. Here, morphological bubble properties are utilized to estimate the bubble velocity and, thus, the bubble size based on its Eötvös number and aspect ratio [11,22]. Furthermore, the bubble size distribution is given by the frequency of occurrence of a respective size class according to

$$H^{(\mathrm{bub})}\left(d_{B,n}\right) = \frac{\sum_b \varepsilon\left(B_b\right)}{\bar{\varepsilon} \cdot \Delta d_B} \qquad \text{with} \quad b \in \left\{1 \ldots N_b \middle| d\left(B_b\right) \in d_{B,n}\right\}. \tag{10}$$

Here, the frequency of occurrence $H^{(\mathrm{bub})}$ for bubble size class $d_{B,n}$ is defined as gas holdup ratio of the sum $\sum_b \varepsilon\left(B_b\right)$ and the time- and space-averaged gas holdup $\bar{\varepsilon}$, divided by bubble size class width Δd_B . The sum is given by each bubble B_b with b being element of the total bubble number N_b and the restriction that the bubble diameter of the respective bubble $d\left(B_b\right)$ belongs to bubble size class $d_{B,n}$. In addition, an alternative representation of the bubble size distribution is given by the probability density function (PDF) that is calculated by applying a kernel density estimation with an interval width of 10%.

Furthermore, redistribution of gas and liquid phase lead to significant lateral bubble movement, especially close to the flow constrictions. Therefore, the transversal movement of each bubbles center of mass is directly tracked for according cross-sectional images, which allows for the determination of its lateral velocity. Subsequently, the lateral velocity field $\bar{u}_{i,j}^{(\mathrm{lat})}$ is derived by void fraction weighted time-averaging of the lateral velocity over each available bubble that crossed the imaging plane during scanning [16].

3 Results

At the beginning of each experiment, deionized water is heated up and circulated through the test section, using the volute pump. In parallel, the pressure is increased by injecting de-oiled gas to the test section until both temperature and pressure reaches stable conditions of 30°C and 4 bar respectively. Subsequently, specific operating conditions are set by adjusting the liquid and gas flow rates as defined by their respective superficial velocity (see Table 2). In total, fifteen steady state operating conditions within the bubbly flow regime are considered for each flow constriction, based on flow maps of Taitel et al. [44]. After a waiting period of about 30 min the UFXCT scans are performed at the different scanning heights, starting at position “A” (see Table 1), for a scanning interval of 15 s. The imaging frequency has been adapted corresponding to the expected flow velocity within the pipe (see Table 2) to obtain a sufficient number of images.

Table 2: Experimental matrix for both flow constrictions based on various combinations of gas and liquid superficial velocities. Highlighted numbers identify the applied UFXCT image frequency f per scanning plane (blue: 1,000 Hz; green: 2,500 Hz).

j_l – liquid superficial velocity / j_g – gas superficial velocity ($m \cdot s^{-1}$)	0.0151	0.0368	0.0898	0.1400
1.6110	#053	#075	-	-
1.0170	#052	#074	#096	#107
0.4050	#050	#072	#094	#105
0.1020	#047	#069	#091	-
0.0405	#045	#067	-	-

As a first analyzing step, the initial flow conditions for each flow constrictions and operating condition are compared. Therefore, the total gas holdup values $\bar{\varepsilon}$ of the four furthest upstream imaging planes (upper and lower UFXCT imaging plane for scanning positions "A" and "B") are compared as the two-phase flow is here undisturbed and fully developed. The corresponding parity plot in Figure 4 shows deviations of $\bar{\varepsilon}$ smaller than ±10%.

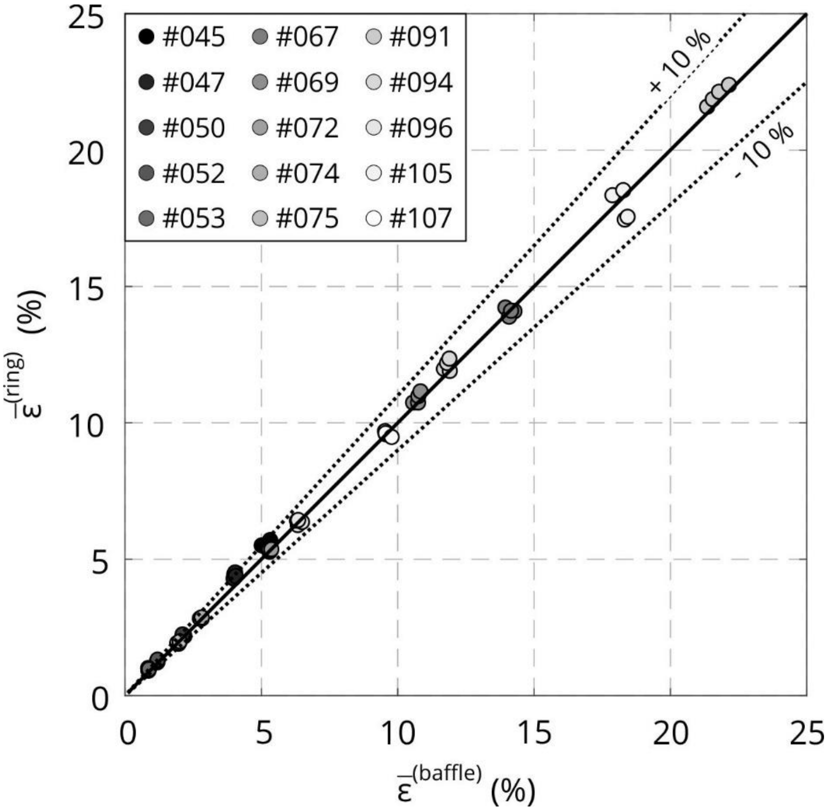

Figure 4: Parity plot of total gas holdup $\bar{\varepsilon}$ values of the undisturbed two-phase flow at the furthest upstream imaging planes of both flow constrictions.

The coefficient of variation reveals a maximum deviation value of 7.16% for the lowest gas holdups. This proves undisturbed two-phase flow conditions upstream of the flow constrictions for each operating point, which is an important quality criterion for CFD comparison and allows for the characterization of the flow constriction impact on the flow field excluding operational influences. Furthermore, the result of the initial flow condition comparison proves the reliability of the introduced image data processing procedure.

3.1 Gas holdup and phase distribution

Figure 5 exemplarily shows sectional views of the gas fraction through the cross-sectional center of the test section pipe (-1 ≤ x/R ≤ 1 for y/R = 0) for both flow constrictions and superficial velocities of j_l = 0.4050 m·s^{-1} and j_g = 0.0368 m·s^{-1}

(#072). In addition, the time-averaged cross-sectional gas fractions $\bar{\varepsilon}_{i,j}$ are shown. The sectional views are perpendicularly arranged to the edge of the baffle-shaped flow constriction and show the linearly interpolated time-averaged gas holdup values obtained at the 18 imaging planes. Such sectional views allow a comparison of both flow constrictions, showing gas accumulations for wide areas of the pipe, especially downstream of the baffle-shaped flow constriction. In contrast, gas is clearly redistributed while passing the blockage, leading to a homogenization of the gas phase distribution far downstream of the flow constriction in case of the ring-shaped type.

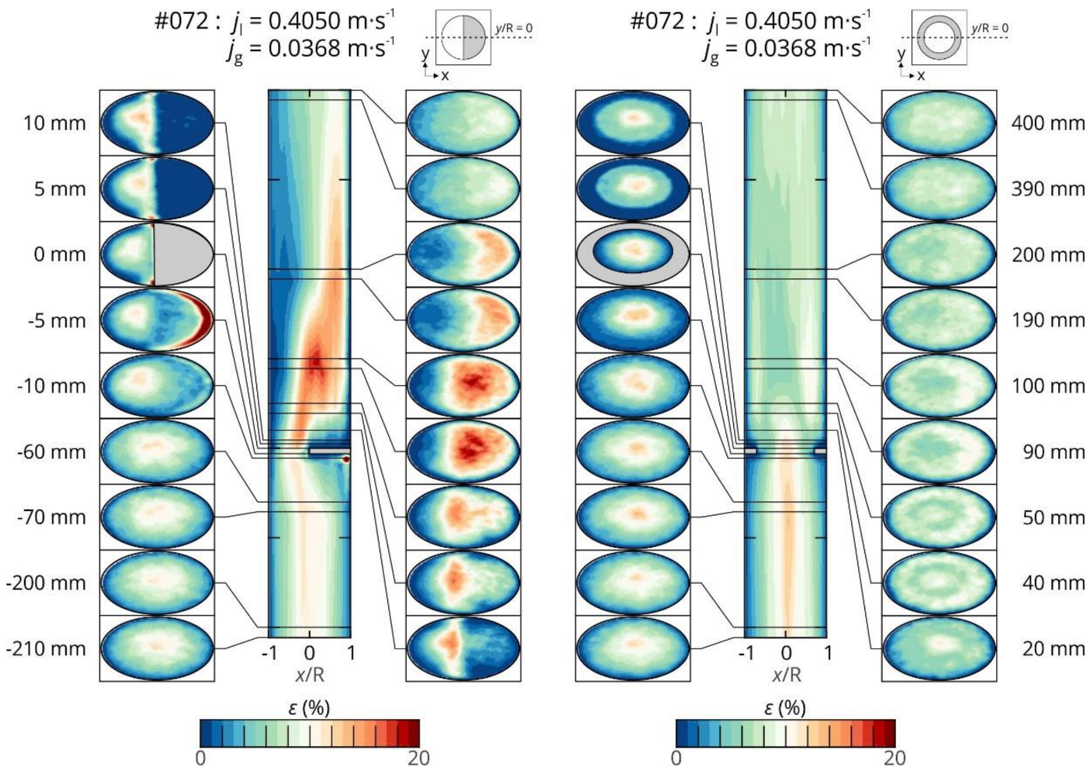

Figure 5: Time-averaged gas fraction sectional views up- and downstream of the baffle-shaped (left) and ring-shaped (right) flow constriction.

Another visualization of determined gas holdup values $\bar{\varepsilon}_{i,j}$ is given in Figure 6. Here, each of the sectional views are additionally normalized to its corresponding averaged total gas holdup $\bar{\varepsilon}^{(\mathrm{AB})}$ of imaging planes "A" and "B" that is also indicated at the top of Figure 6. Thus, the color scaling can be interpreted as the relative amount of gas phase that is distributed along the test section pipe compared to unaffected flow conditions. Hence, this kind of visualization allows detailed investigations on various operating conditions for a given flow constriction. In Figure 6 results for constant gas superficial velocity of j_g = 0.0368 m·s^{-1} and increasing liquid superficial velocities for the baffle-shaped flow constriction are shown.

	#067	#069	#072	#074	#075
j_l	0.0405 m·s^{-1}	0.1020 m·s^{-1}	0.4050 m·s^{-1}	1.0170 m·s^{-1}	1.6110 m·s^{-1}
$\bar{\varepsilon}^{(AB)}$	14.97 %	11.36 %	5.58 %	3.03 %	2.09 %

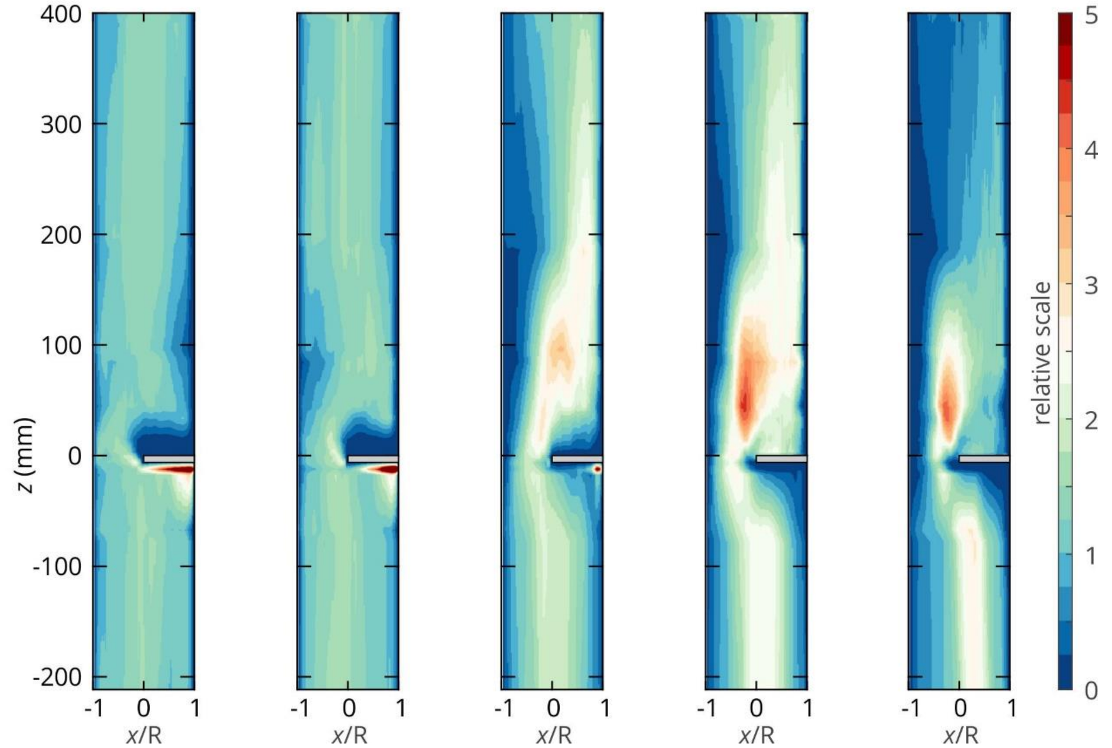

Figure 6: Time-averaged and normalized gas holdup values $\bar{\varepsilon}_{i,j}/\bar{\varepsilon}^{(AB)}$ up- and downstream of the baffle-shaped flow constriction for various superficial liquid velocities j_l and a constant superficial gas velocity of j_g = 0.0368 m·s^{-1}.

It can be concluded that all operating conditions provide symmetric flow profiles for the unaffected region upstream of the flow constriction for z < -60 mm with a maximum at the pipe center. After that, the influence of the half-sided blockage on the phase distribution becomes more and more evident and leads to gas accumulations below the flow constriction for the two lowest superficial liquid velocities (#067, #069) since the redirected liquid flow does not provide enough energy to directly transport the gas phase towards the unobstructed side of the pipe. With increasing superficial liquid velocity the gas accumulation below the flow constriction decreases until it is completely vanished for $j_l \geq 1.0170\ m \cdot s^{-1}$ (#072).

In contrast, gas is accumulated directly downstream of the flow constriction for higher superficial liquid velocities (#072, #074 and #075). This clearly indicates the presence of a recirculation area above the flow constriction that is caused by the strong flow separation at the edge of the flow constriction. For highest superficial liquid velocity $j_l = 1.6110\ m \cdot s^{-1}$ (#075) a large amount of gas accumulates straight above the edge of the flow constriction, which indicates that the momentum of the recirculated liquid is even high enough to displace gas from the recirculation area back to the pipe center. However, no significant recirculating zone is found for the two lowest superficial liquid velocities (#067, #069). Here, the flow almost immediately re-develops to undisturbed pipe flow conditions, whereas significant asymmetric flow fields are found far downstream of the flow constriction for all other operating conditions (#072, #074 and #075). For the latter, gas is clearly redistributed to the obstructed side of the pipe, which is caused by the lower density of gas that is driven out of the accelerated liquid jet.

A more quantitative comparison is shown in Figure 7, where selected gas holdup profiles from representative imaging planes up- and downstream of both flow constrictions are plotted for the same operating conditions as already depicted in Figure 6. For z = -200 mm the comparison of both flow constrictions show similar holdup profiles for all operating conditions, although the overall amount of gas decreases for increasing liquid superficial velocity.

Directly upstream of the baffle-shaped flow constriction at z = -10 mm a gas accumulation zone with approximately twice as much gas as at the unobstructed pipe section is found below the blockage for operating conditions #067 and #069. In contrast, almost no gas is found in this area for all other operating conditions. Here, gas is clearly redistributed to the unobstructed pipe section, where a center peak is developed at $x \approx$ -10 mm. However, no significant stagnation zones or gas redistribution are found for the ring-shaped flow constriction. Considering the higher flow velocity due to the acceleration, the gas holdup is expected to decrease close to the ring-shaped flow constriction. However, the profiles provide nearly the same holdup maxima as for z = -200 mm (by respecting the different scaling). Thus, it can be derived that gas is redistributed to the pipe center, where the superimposition of the acceleration and redistribution effect result in approximately constant gas holdup profiles along the centerline of the pipe.

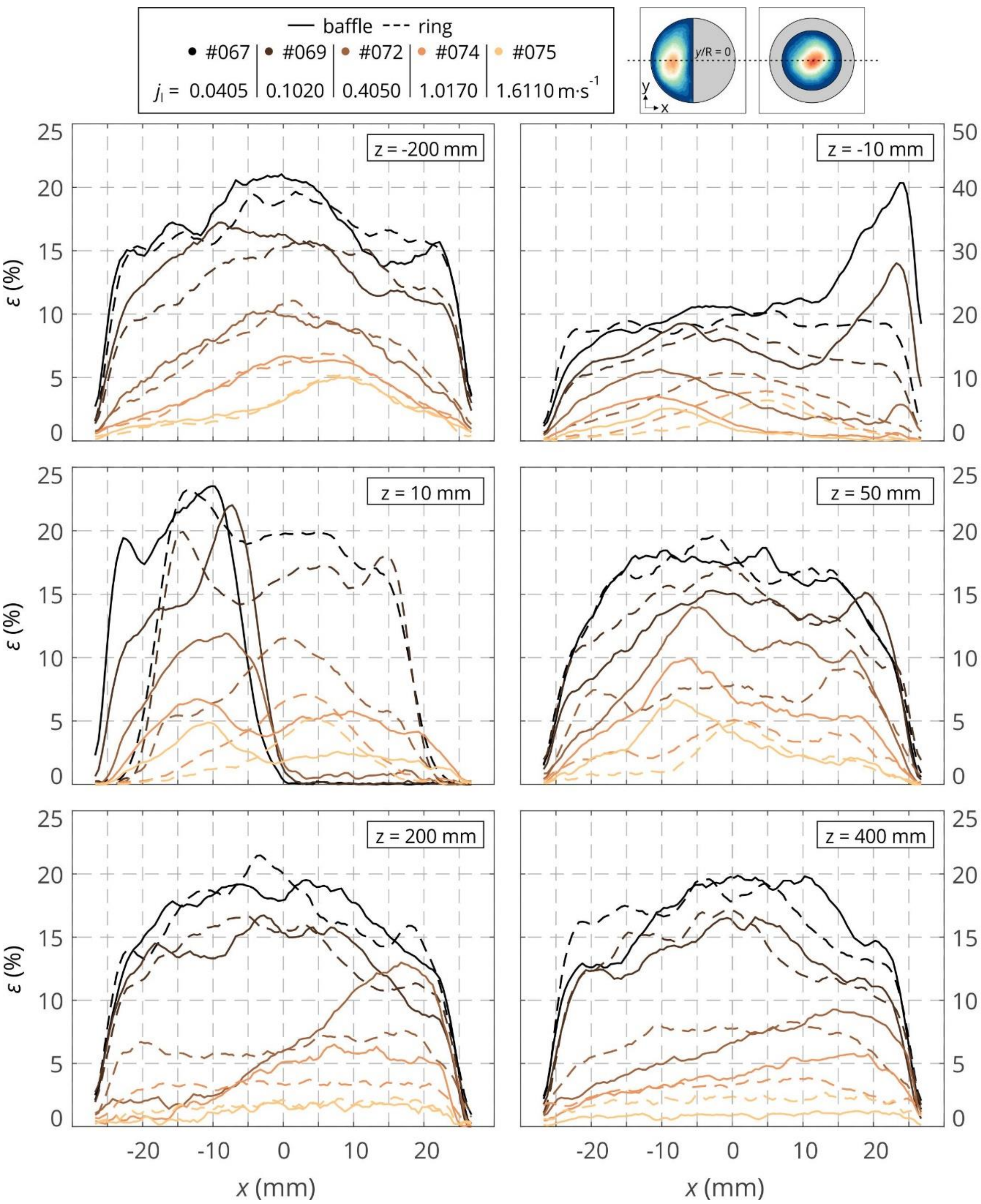

Figure 7: Gas holdup profiles for selected imaging planes up- and downstream of each flow constriction for operating points #067, #069, #072, #074 and #075, showing the effect of increasing liquid superficial velocity j_l.

In the near vicinity downstream of the flow constriction at z = 10 mm gas is clearly redistributed towards the unobstructed pipe section for $j_l \leq 1.0170$ m·s^{-1} and baffle-shaped flow constriction. In contrast, the gas holdup profiles show an additional plateau for higher liquid superficial velocities (#074 and #075), due to the recirculating flow in this area. Furthermore, the maxima of the profiles are slightly eccentric towards the edge of the flow constriction with regard to the unobstructed pipe section. In case of the ring-shaped flow constriction the holdup profiles provide a more narrow distribution of the gas in the pipe center as compared to the upstream condition. Here, the expansion of the flow leads to significant lateral movement of the liquid, which in turn drives the gas towards the pipe center due to its lower density.

At $z = 50$ mm, the flow re-develops for operating conditions #067 and #069, independent of the flow constriction. On the other hand, the recirculating flow causes a maximum of the holdup profiles between -8 mm ≤ x ≤ -5 mm for higher liquid superficial velocities (#072, #074 and #075) in case of the baffle-shaped flow constriction. In contrast, not only a center peak, but also two peaks near the pipe wall are found in cases of the ring-shaped flow constriction for operating conditions #072 and #074. The latter are caused by recirculating flow in the wake region of the flow constriction. However, this recirculation is less pronounced than for baffle-shaped type and is furthermore not noticeable for operating point #075.

Further downstream at $z = 200$ mm and $z = 400$ mm the gas holdup profiles indicate that the two-phase flow is fully re-developed for operating conditions #067 and #069 for both flow constrictions and no significant redistributions of the gas are noticeable compared to the unaffected upstream conditions. In contrast, the flow seems to be also re-developed for higher liquid superficial velocities (#072, #074 and #075) and the ring-shaped flow constriction, but with a persisting difference in the gas distribution, since no significant peaks are found as in case of unaffected upstream conditions. On the other hand, a clear redistribution of the gas towards the obstructed side of the pipe cross-section is still present for those liquid superficial velocities in case of baffle-shaped flow constriction.

Although the peaks decay for increasing relative distances, the flow requires longer distances to re-develop for these operating conditions.

3.2 Bubble sizes

The impact of both, baffle-shaped and ring-shaped flow constriction, on bubble sizes and their distribution is shown in Figure 8 for a bubble size class width of Δd_B = 0.5 mm, again for the same operating conditions and imaging planes as described in Figure 6. For better visual interpretation of the results, the bubble size distributions of operating conditions #072, #074 and #075 are additionally shown in the rescaled inset plots. A comparison of the undisturbed two-phase flow at relative distance z = -200 mm reveals no change of the bubble size distribution for both investigated flow constrictions. A most probable bubble diameter of d_B ≈ 6.0 mm can be identified for all cases, which was already observed by Banowski et al. [22]. Thus, on the one hand it can be assumed that the gas injector produces bubbles of comparable size over a wide range of inlet conditions and, on the other hand, that the flow is fully developed for all considered operating conditions. However, even smaller bubbles might be expected for highest liquid superficial velocities, where higher shear forces and thus higher bubble break-up is expected. In the near vicinity upstream of the flow blockage at z = -10 mm the bubble size distribution is similar to the undisturbed upstream flow condition for operating conditions #067, #069 and #072 for both flow constrictions. Slightly larger bubbles are found for operating point #074 and both flow constrictions, as well as operating point #075 in case of the rings-shaped flow constriction. Here, the sudden reduction of the test section pipe leads to increased lateral movement of the two-phase flow and, thus, a redistribution of the gas towards the unblocked pipe cross-section or pipe center in case of baffle-shaped or ring-shaped flow constriction respectively. Thus, bubble coalescence becomes more probable. In contrast, two peaks of the bubble size distribution are found for operating point

#075 and baffle-shaped flow constriction. Here, the liquid velocity gradients cause high shear forces that additionally split bubbles. The superposition of both effects, break-up and coalescence respectively, lead to most probable bubble sizes of 4.5 mm and 7.0 mm.

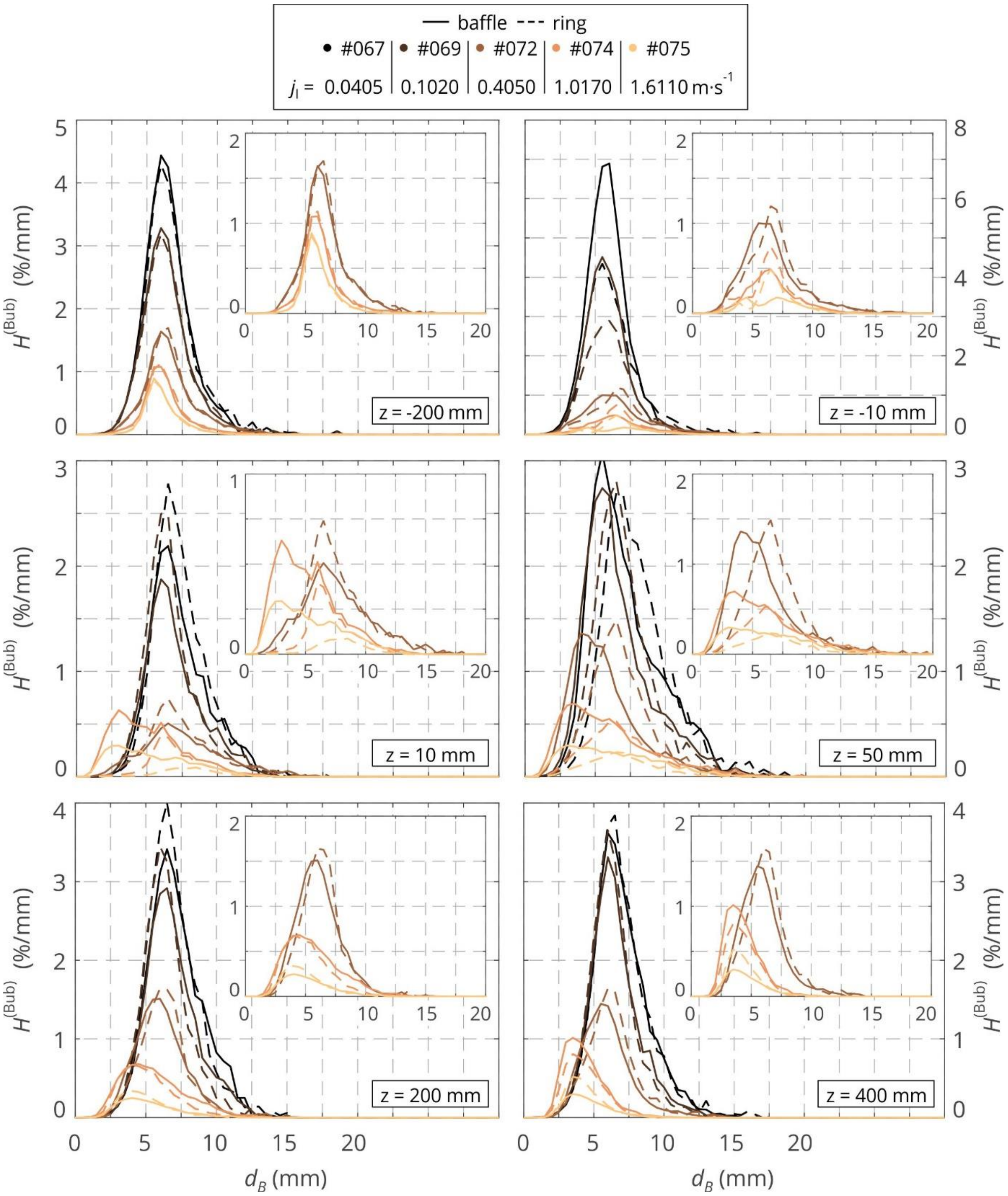

Figure 8: Bubble size distribution as frequency of occurrence $H^{(\mathrm{Bub})}$ for selected imaging planes up- and downstream of each flow constriction for operating points #067, #069, #072, #074 and #075, showing the effect of increasing liquid superficial velocity j_l. For better visual interpretation, insets represent a close-up view of operating points #072, #074 and #075.

Directly downstream of the flow constriction at $z = 10$ mm, the bubble size distribution for operating conditions #067, #069 and #072 shows no significant difference as compared to the undisturbed flow for both flow constrictions. However, slightly higher amount of bubbles with d_B ≤ 4.0 mm are found in case of baffle-shaped flow constriction and at operating point #072, which are caused by the higher shear of the accelerated flow. Furthermore, the bubble size distribution provides a peak at smaller bubbles of d_B ≈ 3.0 mm and also a wider distribution for operating conditions #074 and #075 in case of baffle-shaped flow constriction. In contrast, less but larger bubbles are found for the same operating conditions and ring-shaped flow constriction. Thus, the symmetric reduction of the cross-section causes less break-up of bubbles but higher coalescence rates at this relative distance to the flow constriction.

At z = 50 mm, the recirculation of the flow causes a wider distribution of the bubble sizes, as well as a most probable bubble size of 4.0 mm, 3.5 mm and 3.0 mm for baffle-shaped flow constriction and operating conditions #072, #074 and #075, respectively. This is an explicit indicator for the complex interaction of break-up and coalescence effects in the recirculation area in the wake of the baffle-shaped flow constriction. Furthermore, the bubble size distribution is slightly shifted towards smaller bubbles for the same three operating conditions in case of the ring-shaped flow constriction, since gas is already redistributed towards the pipe wall and, thus, more bubble break-up occurs. In contrast, operating conditions #067 and #069 show slightly higher amounts of larger bubbles with d_B = 8.0 … 14.0 mm for both flow constrictions. Further downstream of the flow constriction (z = 200 mm and 400 mm) the bubble size distribution shows no significant changes but a slight increase of larger bubbles for operating conditions #067 and #069 due to the reduced static pressure within the test section. Furthermore, the bubble size distribution for operating point #072 is approximately equal to the undisturbed upstream flow but with slightly smaller most probable bubble size of d_B ≈ 5.5 mm, also for both flow constrictions. Thus, in terms of bubble sizes the two-phase flow has already re-developed at

z = 200 mm, although the gas is still redistributed as shown in Figure 7. In contrast, bubble sizes are further decreased, resulting in a left skewed distribution for operating conditions #074 and #075 in case of both flow constrictions. Here, the high shear forces are still producing higher break-up rates of the bubbles and the flow has not yet reached stable flow conditions.

In Figure 9 the bubble size distribution is shown as probability density function (PDF) for all imaging planes and operating points #069 and #074. It shows the development of the bubble size distribution up- and downstream of the baffle-shaped flow constriction. Additionally, the averaged bubble diameter $\bar{d}_B$ is indicated as black vertical line for each distribution. In case of operating point #069, no significant changes of the shape of the bubble size distribution as well as the mean bubble diameter is discovered over the entire test section, which is similar to results of the frequency of occurrence presented in Figure 8. In contrast, a clear impact of the baffle-shaped flow constriction on the bubble size distribution is found for operating point #074. On the one hand, the averaged bubble diameter $\bar{d}_B$ clearly decreases downstream of the flow constriction, verifying the increased bubble break-up also in terms of the PDF. On the other hand, the change of shape from mono- to bi-modal distribution (and vise-versa) of the bubble size in the recirculation zone behind the flow constriction is clearly provable (z = 5...50 mm). Subsequently, bubble sizes of operating point #074 show narrower distributions as compared to operating point #069 for unaffected upstream as well as far downstream flow conditions.

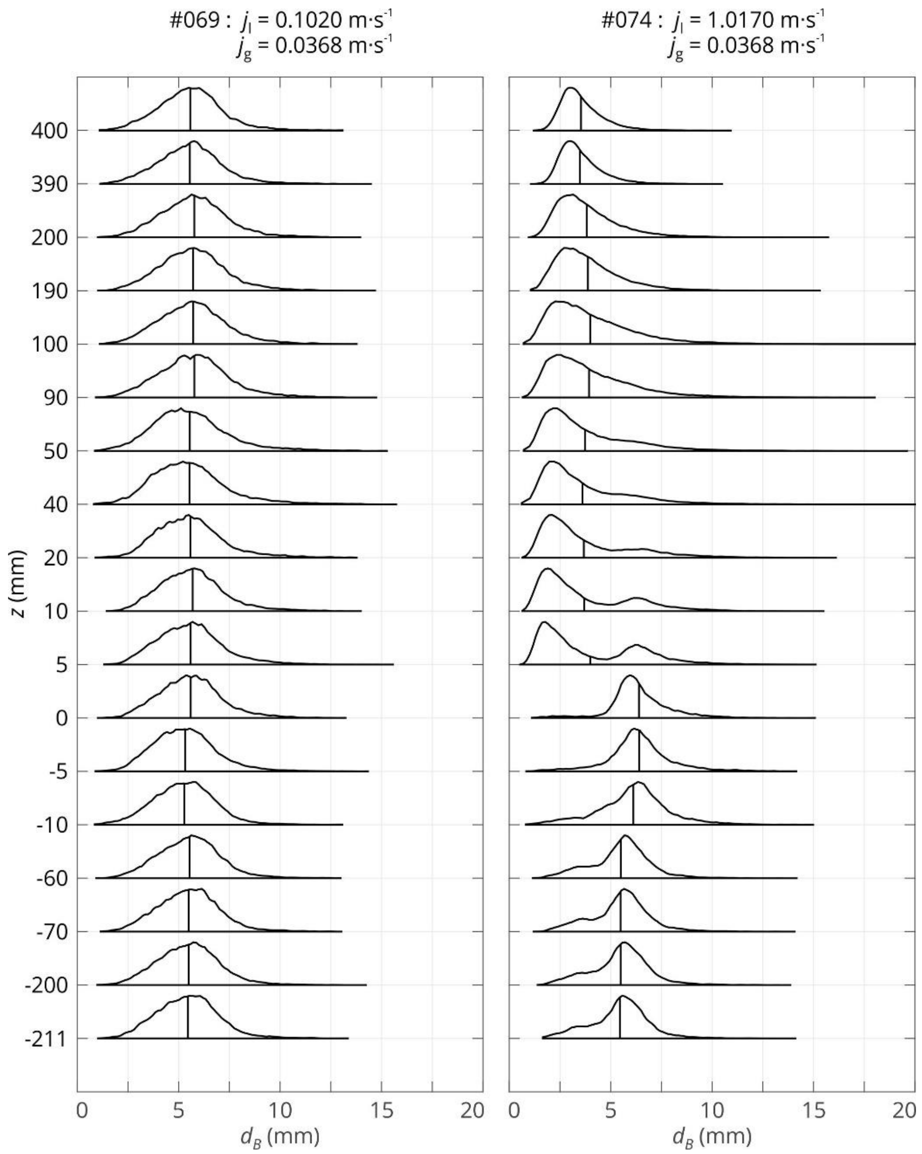

Figure 9: Bubble size distribution as probability density function for all imaging planes up- and downstream of the baffle-shaped flow constriction and operating points #069 and #074.

In Table 3, mean bubble diameters for undisturbed flow $\bar{d}_B^{(\mathrm{in})}$ and affected flow $\bar{d}_B^{(\mathrm{out})}$ for both flow constrictions are shown for the same operating conditions as in Figure 8. Here, $\bar{d}_B^{(\mathrm{in})}$ and $\bar{d}_B^{(\mathrm{out})}$ represent the averaged mean diameter of the four upstream imaging planes of scanning positions “A”, “B” and of the two downstream imaging planes of scanning positon “I”, respectively. Eventually, the change in mean bubble size is defined as $\bar{d}_B^{(\mathrm{ratio})} = \bar{d}_B^{(\mathrm{out})}/\bar{d}_B^{(\mathrm{in})}$. It can be seen, that $\bar{d}_B^{(\mathrm{in})}$ is approximately equal for all operating conditions, whereas $\bar{d}_B^{(\mathrm{out})}$ clearly decreases with increasing liquid superficial velocity. No influence of the flow constriction is recognizable for operating condition #067, where the mean bubble size increases because of the decreased static pressure within the test section. Interestingly, the mean bubble diameter is influenced in the same way for both flow constrictions, despite the different bubble size distributions as discussed for Figure 8.

Table 3: Mean bubble diameter $\bar{d}_B$ for operating points #067, #069, #072, #074 and #075, showing the effect of increasing liquid superficial velocity j_l. The listed values represent averaged data for undisturbed flow upstream $\bar{d}_B^{(\mathrm{in})}$ and affected flow downstream $\bar{d}_B^{(\mathrm{out})}$ of each flow constriction, as well as their ratio $\bar{d}_B^{(\mathrm{ratio})}$.

	baffle-shaped constriction					ring-shaped constriction				
	#067	#069	#072	#074	#075	#067	#069	#072	#074	#075
$\bar{d}_B^{(\mathrm{in})}$	5.68	5.50	5.59	5.49	5.69	5.69	5.54	5.68	5.51	5.69
$\bar{d}_B^{(\mathrm{out})}$	5.83	5.57	4.96	3.52	3.60	5.88	5.58	5.27	3.65	3.72
$\bar{d}_B^{(\mathrm{ratio})}$	1.03	1.01	0.89	0.64	0.63	1.03	1.01	0.93	0.66	0.65

3.3 Lateral bubble velocities

In the following, calculated lateral bubble velocity fields for selected imaging planes up- and downstream of the baffle-shaped flow constriction are discussed for operating conditions #069 (Figure 10) and #074 (Figure 11). Both operating conditions represent two main distinct flow fields that are found in all investigated operating conditions: a) flow fields with gas accumulation upstream of the baffle-shaped flow constriction, but nearly no recirculating flow downstream of it and b) a strong recirculating flow in the wake of the flow constriction for higher liquid superficial velocities. For better visualization, the magnitude of lateral bubble velocity is given by colored image plots, whereas the direction is given by normalized velocity vectors.

In Figure 10 the lateral bubble velocity field of operating point #069 with lower liquid superficial velocity of $j_1 = 0.1020$ m·s^{-1} is shown. In case of unaffected two-phase flow at maximum distance upstream of the baffle-shaped flow constriction only low lateral bubble velocity and, thus, lateral movement of the bubbles is found. The velocity vectors point mainly outwards from the center of the pipe because the lateral movement is dominated by bubbles with d_B < 5.5 mm, which move towards the pipe wall due to the lift force. The lateral movement clearly increases in the direct vicinity upstream of the flow constriction at z = -10 mm. Here, both radial and azimuthal bubble movement is found, which appears to be counteractive regarding the center plane of the pipe that is perpendicular to the edge of the flow constriction. Following the flow progress, at z = -6 mm, bubbles mainly move towards the unobstructed pipe section which is also found at the center height of the flow constriction. After passing the flow constriction, two distinct zones with approximately equal lateral bubble velocity are found. The velocity vectors show both movement towards the unobstructed and the obstructed pipe section. Interestingly, both zones are separated by a defined line of zero bubble velocity, which moves from the edge of the flow constriction towards the periphery of the unobstructed pipe section from at z = 0 mm to 50 mm, respectively. In this course, bubble movement towards the obstructed pipe section becomes more dominant with a clear maximum at z = 50 mm. Further downstream, the lateral bubble velocity field shows again unaffected behavior in terms of velocity magnitude and vectors.

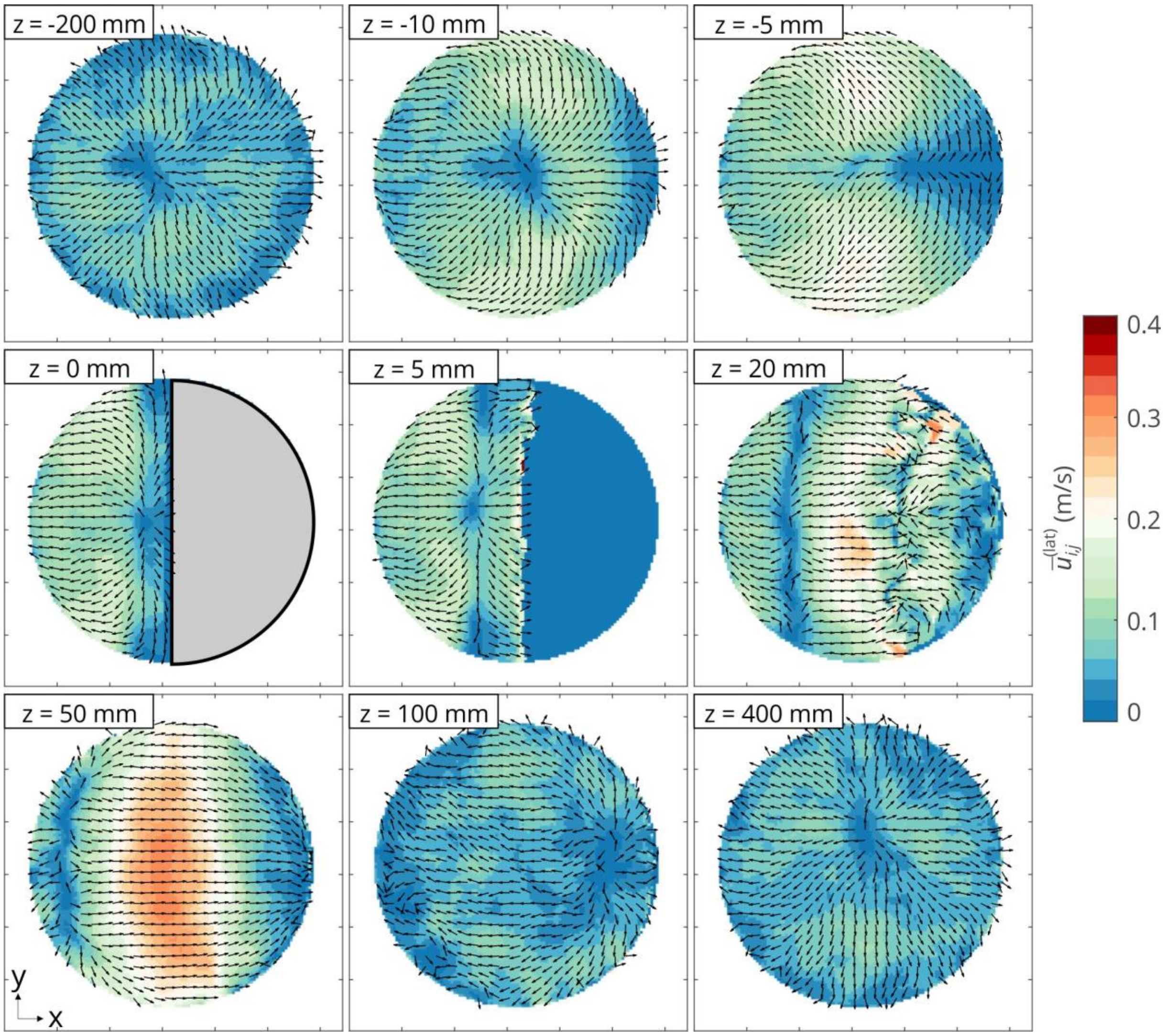

Figure 10: Lateral bubble velocity fields for selected imaging planes up- and downstream of the baffle-shaped flow constriction for operating point #069 with j_l = 0.1020 m·s^{-1} und j_g = 0.0368 m·s^{-1}. The color scaling shows the magnitude and the arrows show the velocity vectors of the lateral bubble velocity (velocity vectors are normalized for better visualization).

In contrast, Figure 11 shows lateral bubble velocity fields for operating point #074 with higher liquid superficial velocity of j_l = 1.0170 m·s^{-1}. Although the lateral bubble velocity is higher for unaffected two-phase flow at maximum distance to the flow constriction, the direction of the velocity vectors is comparable to operating point #069. However, the liquid velocity gradient between center and wall region is steeper whereby the lateral bubble velocities rise correspondingly. Close to the flow constriction, the lateral movement clearly increases again.

However, in contrast to operating point #069 velocity vectors mainly point towards the unobstructed pipe section with less azimuthal movement.

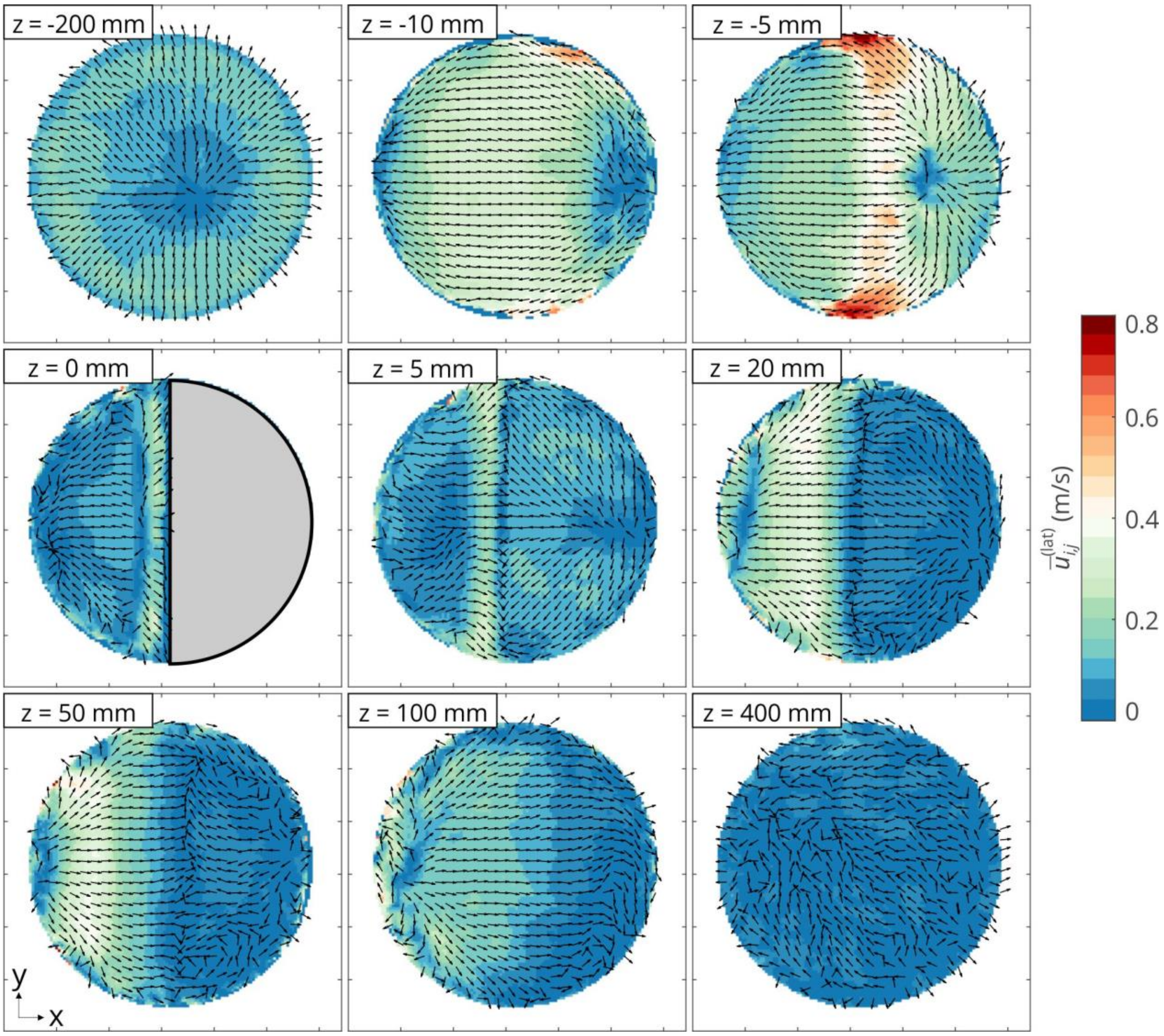

Figure 11: Lateral bubble velocity fields for selected imaging planes up- and downstream of the baffle shaped flow constriction for operating point #074 with j_l = 1.0170 m·s^{-1} und j_g = 0.0368 m·s^{-1}. The color scaling shows the magnitude and the arrows show the velocity vectors of the lateral bubble velocity (velocity vectors are normalized for better visualization).

By passing the flow constriction at z = 0 mm, only low lateral movement is found and bubbles tend to move to the edge of the flow constriction.

In the following downstream wake region from z = 0 mm to 50 mm recirculating flow with negative axial liquid velocity is found at the obstructed pipe section. This velocity is, however, lower than for the unobstructed pipe section, which forces bubbles mainly towards the centerline of the pipe straight above the edge of the flow constriction. In contrast, nearly no lateral movement is found in the downward flow, especially at z = 20 mm and 50 mm, and the bubble velocity vectors indicate only statistical fluctuations, and, thus, no clear directed movement. At z = 100 mm bubbles move towards the obstructed pipe section, which indicates that no recirculating flow affects the lateral movement anymore. Further downstream at z = 400 mm, the lateral bubble velocity field shows only statistical movement and rather low velocities of bubbles.

4 Conclusion

We experimentally studied the two-phase flow around two different flow constrictions using UFXCT imaging technique. A baffle-shaped and a ring-shaped type of flow constriction were used to induce generic three-dimensional flow fields in a vertical DN50 pipe. We studied the flow at various gas and liquid superficial velocities in vertical co-current upward flow under nearly adiabatic conditions. From UFXCT technique phase distributions and bubble sizes were obtained with high temporal and spatial resolution. Therefore, an enhanced data processing procedure was developed to increase the reliability of the image data. The data is available as a benchmark data set at the Rossendorf Data Repository (RODARE) [30,31].

In this paper, we exemplarily analyzed flow conditions for the cases of varying liquid superficial velocities and fixed gas superficial velocity of j_g = 0.0368 m·s^{-1}. In case of baffle-shaped flow constriction, sectional views of the time-averaged gas holdup revealed the change of gas accumulation from upstream to downstream position with increasing liquid superficial velocity. In case of ring-shaped flow constriction less gas accumulation was found. However, the bubble size distribution as well as the mean bubble diameter showed similar trends along the test section pipe for both flow constrictions. Eventually, lateral bubble velocity fields for the baffle-shaped flow constriction revealed clear lateral movement of the bubbles downstream of the constriction towards the obstructed side of the test section pipe in case of lower liquid superficial velocity. In contrast, nearly no lateral movement was found in this area, but directly upstream of the constriction in case of higher liquid superficial velocity.

5 Acknowledgments

This work is funded by the German Federal Ministry for Economic Affairs and Energy (BMWi) with the grant number 1501481 on the basis of a decision by the German Bundestag.

6 Nomenclature

Latin letters	
a	offset for calculation of $\bar{\mu}_{i,j}^{(\mathrm{gas})}$
B	single identified Bubble
D and d	diameter (mm)
f	image frequency per scanning plane
F	cross-correlation function
H	frequency of occurrence (%/mm)
j	superficial velocity (m·s^{-1})
L and l	length (mm)
Δm	plane distance map (mm)
N	total number
R	radius (mm)

Δt	time shift (ms)
u	velocity ($m \cdot s^{-1}$)
w	pixel weights
x, y	space coordinates (mm)
z	relative measurement height (mm)
Greek letters	
ε	gas holdup (%)
ε_m	mean value of Gaussian distribution function fitted to gas holdup histogram
μ	attenuation coefficient in (mm^{-1})
μ_μ	mean value of Gaussian distribution
Super- and subscripts	
ax	axial
b	bubble identifier
B	bubble
bin	binarized data set
gas and g	gaseous phase
Id	identifier data set
i, j	space coordinates (pixel)
k	time coordinate (ms)
lat	lateral
liq and l	liquid phase
low and up	scanning plane identifier
ref	reference pixel

tp	two-phase flow data set

7 References

[1] D. Bestion, Applicability of two-phase CFD to nuclear reactor thermalhydraulics and elaboration of Best Practice Guidelines, Nucl. Eng. Des. 253 (2012) 311–321. https://doi.org/10.1016/j.nucengdes.2011.08.068.

[2] D. Bestion, The difficult challenge of a two-phase CFD modelling for all flow regimes, Nucl. Eng. Des. 279 (2014) 116–125. https://doi.org/10.1016/j.nucengdes.2014.04.006.

[3] D. Lucas, R. Rzehak, E. Krepper, T. Ziegenhein, Y. Liao, S. Kriebitzsch, P. Apanasevich, A strategy for the qualification of multi-fluid approaches for nuclear reactor safety, Nucl. Eng. Des. 299 (2016) 2–11. https://doi.org/10.1016/j.nucengdes.2015.07.007.

[4] H.-M. Prasser, Evolution of interfacial area concentration in a vertical air–water flow measured by wire–mesh sensors, Nucl. Eng. Des. 237 (2007) 1608–1617. https://doi.org/10.1016/j.nucengdes.2007.02.024.

[5] S. Hosokawa, A. Tomiyama, Multi-fluid simulation of turbulent bubbly pipe flows, Chem. Eng. Sci. 64 (2009) 5308–5318. https://doi.org/10.1016/j.ces.2009.09.017.

[6] D. Lucas, M. Beyer, J. Kussin, P. Schütz, Benchmark database on the evolution of two-phase flows in a vertical pipe, Nucl. Eng. Des. 240 (2010) 2338–2346. https://doi.org/10.1016/j.nucengdes.2009.11.010.

[7] M. Ishii, S.S. Paranjape, S. Kim, X. Sun, Interfacial structures and interfacial area transport in downward two-phase bubbly flow, Int. J. Multiph. Flow. 30 (2004) 779–801. https://doi.org/10.1016/j.ijmultiphaseflow.2004.04.009.

[8] T. Hibiki, H. Goda, S. Kim, M. Ishii, J. Uhle, Axial development of interfacial structure of vertical downward bubbly flow, Int. J. Heat Mass Transf. 48 (2005) 749–764. https://doi.org/10.1016/j.ijheatmasstransfer.2004.07.045.

[9] G. Wang, Z. Dang, P. Ju, X. Yang, M. Ishii, A. Ireland, S. Bajorek, M. Bernard, Experimental study on interfacial structure and interfacial area transport in downward two-phase flow, Int. J. Heat Mass Transf. 106 (2017) 1303–1317. https://doi.org/10.1016/j.ijheatmasstransfer.2016.10.112.

[10] S.K. Wang, S.J. Lee, O.C. Jones, R.T. Lahey, 3-D turbulence structure and phase distribution measurements in bubbly two-phase flows, Int. J. Multiph. Flow. 13 (1987)

327–343. https://doi.org/10.1016/0301-9322(87)90052-8.

[11] M. Banowski, U. Hampel, E. Krepper, M. Beyer, D. Lucas, Experimental investigation of two-phase pipe flow with ultrafast X-ray tomography and comparison with state-of-the-art CFD simulations, Nucl. Eng. Des. 336 (2018) 90–104. https://doi.org/10.1016/j.nucengdes.2017.06.035.

[12] Z. Dang, Z. Yang, X. Yang, M. Ishii, Experimental study on void fraction, pressure drop and flow regime analysis in a large ID piping system, Int. J. Multiph. Flow. 111 (2019) 31–41. https://doi.org/10.1016/j.ijmultiphaseflow.2018.10.006.

[13] G. Kocamustafaogullari, W.D. Huang, Internal structure and interfacial velocity development for bubbly two-phase flow, Nucl. Eng. Des. 151 (1994) 79–101. https://doi.org/10.1016/0029-5493(94)90035-3.

[14] J.D. Talley, T. Worosz, S. Kim, Characterization of horizontal air–water two-phase flow in a round pipe part II: Measurement of local two-phase parameters in bubbly flow, Int. J. Multiph. Flow. 76 (2015) 223–236. https://doi.org/10.1016/j.ijmultiphaseflow.2015.06.012.

[15] P. Wiedemann, A. Döß, E. Schleicher, U. Hampel, Fuzzy flow pattern identification in horizontal air-water two-phase flow based on wire-mesh sensor data, Int. J. Multiph. Flow. 117 (2019) 153–162. https://doi.org/10.1016/j.ijmultiphaseflow.2019.05.004.

[16] H.-M. Prasser, M. Beyer, T. Frank, S. Al Issa, H. Carl, H. Pietruske, P. Schütz, Gas–liquid flow around an obstacle in a vertical pipe, Nucl. Eng. Des. 238 (2008) 1802–1819. https://doi.org/10.1016/j.nucengdes.2007.11.007.

[17] T. Frank, H.-M. Prasser, M. Beyer, S. Al Issa, Gas-Liquid Flow around an Obstacle in a Vertical Pipe – CFD Simulation & Comparison to Experimental Data, in: 6th Int. Conf. Multiph. Flow, ICMF 2007, Leipzig, 2007: pp. 1–14.

[18] H.-M. Prasser, A. Böttger, J. Zschau, A new electrode-mesh tomograph for gas–liquid flows, Flow Meas. Instrum. 9 (1998) 111–119. https://doi.org/10.1016/S0955-5986(98)00015-6.

[19] H. Pietruske, H.-M. Prasser, Wire-mesh sensors for high-resolving two-phase flow studies at high pressures and temperatures, Flow Meas. Instrum. 18 (2007) 87–94.

https://doi.org/10.1016/j.flowmeasinst.2007.01.004.

[20] E. Krepper, M. Beyer, T. Frank, D. Lucas, H.-M. Prasser, CFD modelling of polydispersed bubbly two-phase flow around an obstacle, Nucl. Eng. Des. 239 (2009) 2372–2381. https://doi.org/10.1016/j.nucengdes.2009.06.015.

[21] H.-M. Prasser, M. Misawa, I. Tiseanu, Comparison between wire-mesh sensor and ultra-fast X-ray tomograph for an air–water flow in a vertical pipe, Flow Meas. Instrum. 16 (2005) 73–83. https://doi.org/10.1016/j.flowmeasinst.2005.02.003.

[22] M. Banowski, M. Beyer, L. Szalinski, D. Lucas, U. Hampel, Comparative study of ultrafast X-ray tomography and wire-mesh sensors for vertical gas–liquid pipe flows, Flow Meas. Instrum. 53 (2017) 95–106. https://doi.org/10.1016/j.flowmeasinst.2016.02.001.

[23] F. Fischer, D. Hoppe, E. Schleicher, G. Mattausch, H. Flaske, R. Bartel, U. Hampel, An ultra fast electron beam x-ray tomography scanner, Meas. Sci. Technol. 19 (2008) 094002. https://doi.org/10.1088/0957-0233/19/9/094002.

[24] F. Fischer, U. Hampel, Ultra fast electron beam X-ray computed tomography for two-phase flow measurement, Nucl. Eng. Des. 240 (2010) 2254–2259. https://doi.org/10.1016/j.nucengdes.2009.11.016.

[25] S. Rabha, M. Schubert, F. Grugel, M. Banowski, U. Hampel, Visualization and quantitative analysis of dispersive mixing by a helical static mixer in upward co-current gas–liquid flow, Chem. Eng. J. 262 (2015) 527–540. https://doi.org/10.1016/j.cej.2014.09.019.

[26] M. Wagner, J. Zalucky, M. Bieberle, U. Hampel, Hydrodynamic investigations of bubbly flow in periodic open cellular structures by ultrafast X-ray tomography, in: 10th Pacific Symp. Flow Vis. Image Process., Naples, Italy, 2015: pp. 15–18.

[27] A.-E. Sommer, M. Wagner, S.F. Reinecke, M. Bieberle, F. Barthel, U. Hampel, Analysis of activated sludge aerated by membrane and monolithic spargers with ultrafast X-ray tomography, Flow Meas. Instrum. 53 (2017) 18–27. https://doi.org/10.1016/j.flowmeasinst.2016.05.008.

[28] Y.M. Lau, F. Möller, U. Hampel, M. Schubert, Ultrafast X-ray tomographic imaging of multiphase flow in bubble columns – Part 2: Characterisation of bubbles in the dense

regime, Int. J. Multiph. Flow. 104 (2018) 272–285. https://doi.org/10.1016/j.ijmultiphaseflow.2018.02.009.

[29] F. Möller, R. Kipping, C. Lavetty, U. Hampel, M. Schubert, Two-Bubble Class Approach Based on Measured Bubble Size Distribution for Bubble Columns with and without Internals, Ind. Eng. Chem. Res. 58 (2019) 2759–2769. https://doi.org/10.1021/acs.iecr.8b05784.

[30] M. Neumann-Kipping, U. Hampel, Hydrodynamic experimental benchmark data of bubbly two-phase pipe flow around a semi-circular constriction, (2019). https://doi.org/10.14278/RODARE.195.

[31] M. Neumann-Kipping, U. Hampel, Hydrodynamic experimental benchmark data of bubbly two-phase pipe flow around a ring-shaped constriction, (2019). https://doi.org/10.14278/RODARE.197.

[32] A. Schaffrath, A.K. Krüssenberg, F.P. Weiß, E.F. Hicken, M. Beyer, H. Carl, H.M. Prasser, J. Schuster, P. Schütz, M. Tamme, W. Zimmermann, TOPFLOW - A new multipurpose thermalhydraulic test facility for the investigation of steady state and transient two phase flow phenomena, 2001.

[33] H.-M. Prasser, M. Beyer, A. Böttger, H. Carl, D. Lucas, A. Schaffrath, P. Schütz, F.-P. Weiss, J. Zschau, Influence of the Pipe Diameter on the Structure of the Gas-Liquid Interface in a Vertical Two-Phase Pipe Flow, Nucl. Technol. 152 (2005) 3–22. https://doi.org/10.13182/NT05-A3657.

[34] A. Kak, M. Slaney, Principles of Computerized Tomographic Imaging, IEEE Press, New York, 1988.

[35] W.A. Kalender, X-ray computed tomography, Phys. Med. Biol. 51 (2006) R29–R43. https://doi.org/10.1088/0031-9155/51/13/R03.

[36] W.A. Kalender, Computed Tomography: Fundamentals, System Technology, Image Quality, Applications, 3rd edn, Publicis Erlangen, Erlangen, 2011.

[37] U. Hampel, E. Krepper, D. Lucas, M. Beyer, L. Szalinski, M. Banowski, F. Barthel, D. Hoppe, A. Bieberle, T. Barth, High-resolution two-phase flow measurement techniques for the generation of experimental data for CFD code qualification, Kerntechnik. 78

(2013) 9–15. https://doi.org/10.3139/124.110301.

[38] F. Barthel, M. Bieberle, D. Hoppe, M. Banowski, U. Hampel, Velocity measurement for two-phase flows based on ultrafast X-ray tomography, Flow Meas. Instrum. 46 (2015) 196–203. https://doi.org/http://dx.doi.org/10.1016/j.flowmeasinst.2015.06.006.

[39] J. Zalucky, T. Claußnitzer, M. Schubert, R. Lange, U. Hampel, Pulse flow in solid foam packed reactors: Analysis of morphology and key characteristics, Chem. Eng. J. 307 (2017) 339–352. https://doi.org/10.1016/j.cej.2016.08.091.

[40] M. Bieberle, M. Wagner, F. Gücker, M. Neumann, U. Hampel, Advanced correction algorithms for ultrafast X-ray computed tomography, in: Proc. 9th World Congr. Ind. Process Tomogr., Bath, 2018.

[41] M. Banowski, D. Lucas, L. Szalinski, A new algorithm for segmentation of ultrafast X-ray tomographed gas–liquid flows, Int. J. Therm. Sci. 90 (2015) 311–322. https://doi.org/10.1016/j.ijthermalsci.2014.12.015.

[42] M. Beyer, L. Szalinski, E. Schleicher, C. Schunk, Wire-Mesh Sensor Data Processing Software, (2018) 82. http://mpmt.de/de/produkte/gittersensor/de/downloads/wire-mesh-sensor-data-processing-software (accessed May 11, 2018).

[43] M. Neumann, M. Bieberle, M. Wagner, A. Bieberle, U. Hampel, Improved axial plane distance and velocity determination for ultrafast electron beam x-ray computed tomography, Meas. Sci. Technol. 30 (2019) 084001. https://doi.org/10.1088/1361-6501/ab1ba2.

[44] Y. Taitel, D. Bornea, A.E. Dukler, Modelling flow pattern transitions for steady upward gas-liquid flow in vertical tubes, AIChE J. 26 (1980) 345–354. https://doi.org/10.1002/aic.690260304.